A COMPREHENSIVE X-RAY ABSORPTION MODEL FOR ATOMIC OXYGEN

T. W. Gorczyca[1], M. A. Bautista[1], M. F. Hasoglu[2], J. García[3], E. Gatuzz[4], J. S. Kaastra[5,6], T. R. Kallman[7],
S. T. Manson[8], C. Mendoza[1,4], A. J. J. Raassen[5,9], C. P. de Vries[5], and O. Zatsarinny[10]

[1] Department of Physics, Western Michigan University, Kalamazoo, MI 49008, USA
[2] Hasan Kalyoncu University, 27100 Sahinbey, Gaziantep, Turkey
[3] Harvard-Smithsonian Center for Astrophysics, MS-6, 60 Garden Street, Cambridge, MA 02138, USA
[4] Centro de Física, Instituto Venezolano de Investigaciones Científicas, Caracas 1020, Venezuela
[5] SRON Netherlands Institute for Space Research, Sorbonnelaan 2, 3584-CA Utrecht, The Netherlands
[6] Sterrenkundig Instituut, Universiteit Utrecht, P.O. Box 80000, 3508-TA Utrecht, The Netherlands
[7] NASA Goddard Space Flight Center, Greenbelt, MD 20771, USA
[8] Department of Physics and Astronomy, Georgia State University, Atlanta, GA 30303, USA
[9] Astronomical Institute Anton Pannekoek, University of Amsterdam, Science Park 904, 1098-XH Amsterdam, The Netherlands
[10] Department of Physics and Astronomy, Drake University, Des Moines, IA 50311, USA

ABSTRACT

An analytical formula is developed to accurately represent the photoabsorption cross section of O I for all energies of interest in X-ray spectral modeling. In the vicinity of the K edge, a Rydberg series expression is used to fit *R*-matrix results, including important orbital relaxation effects, that accurately predict the absorption oscillator strengths below threshold and merge consistently and continuously to the above-threshold cross section. Further, minor adjustments are made to the threshold energies in order to reliably align the atomic Rydberg resonances after consideration of both experimental and observed line positions. At energies far below or above the K-edge region, the formulation is based on both outer- and inner-shell direct photoionization, including significant shake-up and shake-off processes that result in photoionization-excitation and double-photoionization contributions to the total cross section. The ultimate purpose for developing a definitive model for oxygen absorption is to resolve standing discrepancies between the astronomically observed and laboratory-measured line positions, and between the inferred atomic and molecular oxygen abundances in the interstellar medium from XSTAR and SPEX spectral models.

Key words: atomic processes – ISM: atoms – line: formation – line: profiles – X-rays: ISM

Online-only material: color figures

1. INTRODUCTION

Atomic photoionization, an important astrophysical process, has been studied for more than a century—since the seminal understanding of its energetics by Einstein (1905) and the first calculations of quantum mechanical cross sections (Bates 1939). Over the years, a plethora of experimental and theoretical investigations have managed an excellent grasp of its physics (Fano & Cooper 1968; Starace 1982), together with a remarkable quantitative description of the valence-shell photoionization of atoms and atomic ions (Opacity Project Team 1995, 1997). However, the quantitative model of inner-shell photoabsorption is less sound because of a variety of relaxation processes, namely Auger and X-ray emission, that must be taken into account to achieve acceptable accuracy, especially in the near-threshold region.

Inner-shell photoabsorption of metals with nuclear charge $7 \leqslant Z \leqslant 28$ is directly accessible to modern X-ray observatories, such as *Chandra* and *XMM-Newton*, and, hence, is of much interest in astronomy. Particularly prominent in the photoabsorption of the interstellar medium (ISM) are the K-shell features (lines and edges) of atomic oxygen, which are the most abundant metal and is critically important in the energetic and chemical evolution of the universe (Stasińska et al. 2012). At present, though, the unsatisfactory quantitative understanding of oxygen inner-shell photoabsorption is such that there exist various sets of cross sections, each one leading to different conclusions regarding the ionization and atomic-to-molecular fractions in the ISM along various Galactic lines of sight.

The first inner-shell photoabsorption cross sections of oxygen reported (Henke et al. 1993; Verner et al. 1993; Verner & Yakovlev 1995) were simple step-function fits to low-resolution solid-state data (Henke et al. 1993) or to theoretical calculations by Reilman & Manson (1979) using a central potential method. These results depict cross sections across inner-shell thresholds with unphysical, discontinuous edges where even the threshold energies are poorly determined. These cross sections were used by Schulz et al. (2002) in an early analysis of ISM absorption near the oxygen K edge in *Chandra* X-ray binary-star spectra.

A later theoretical cross section, which took into account resonance effects, was computed by McLaughlin & Kirby (1998) using the *R*-matrix technique. However, this calculation failed to include the effects of orbital relaxation and spectator Auger damping, which causes blending of the resonances converging to the inner-shell thresholds, thus smearing the otherwise sharp K-shell edge. Both Paerels et al. (2001) and Takei et al. (2002) used this cross section to analyze the ISM K-shell absorption of oxygen in the *Chandra* spectra toward X0614+091 and Cyg X-2, respectively. All these studies found, after fitting the O I Kα line and edge, residual narrow absorption at ≈23.36 Å and a broad edge feature at ≈22.9 Å. In all cases, the residual absorption was most likely attributed to oxygen compounds, although the narrow absorption feature could also be due to O II.

By contrast, de Vries et al. (2003), using the *XMM-Newton* Reflection Grating Spectrometer (RGS), found that the ISM oxygen K-shell edge observed in X-ray binaries and extragalactic sources was well described by the *R*-matrix cross section of

McLaughlin & Kirby (1998). A second *R*-matrix calculation of the O I cross section was reported by Gorczyca & McLaughlin (2000), with a full account of relaxation and Auger damping, in fairly good agreement with the laboratory measurements of Stolte et al. (1997). As a result, Juett et al. (2004) analyzed the *Chandra* spectra available at the time using the cross sections by both McLaughlin & Kirby (1998) and Gorczyca & McLaughlin (2000). They point out that the *R*-matrix cross sections and those by Verner et al. (1993) and Verner & Yakovlev (1995) agreed to within ≈5% well above threshold, but with significant differences in the threshold region. These differences were such that, when using the more recent cross section to fit the spectrum, the previously found broad threshold residuals disappeared. Thus, it was concluded that the narrow absorption feature in the spectra, after subtracting the O I contribution, was due to trace amounts of ionized oxygen rather than to molecular compounds. Juett et al. (2004) also found that the discrepancies between the various calculations and experiments regarding the wavelengths of the O I Kα line and the K-shell threshold were considerably greater than the resolution of the astronomical spectra. Therefore, this energy dispersion may be the main source of uncertainty left in the atomic cross sections.

Since then, García et al. (2005) have reported *R*-matrix calculations for the whole oxygen isonuclear sequence, which, in the case of O I, agree to within ≈10% with the near-threshold cross section of Gorczyca & McLaughlin (2000). Subsequently, García et al. (2011) used these datasets to reanalyze seven *XMM-Newton* observations of the X-ray binary Sco X-1, and, by adjusting the absolute wavelength scale of the theoretical cross sections, found that the spectra were well fitted by O I absorption alone with no conclusive evidence of contributions from any other source. On the other hand, a thorough study of *XMM-Newton* spectra toward the low-mass binary GS 1826−238 by Pinto et al. (2010) showed that the ISM was composed of a mixture of multi-phase gas, dust, and molecules; in the case of oxygen, its abundance was found to be 20–30% higher than protosolar, and at least 10% of its column density was in the form of molecules and dust grains. These findings have been confirmed by Pinto et al. (2013) in a more extensive survey of nine low-mass X-ray binaries where 15–25% of the total amount of oxygen was found to be condensed in dust. Moreover, in a recent examination of several *Chandra* spectra toward the low-mass binary XTE J1817−330, Gatuzz et al. (2013) were forced to shift the photoionization cross sections of García et al. (2005) to fit the absorption lines from both the high- (O VI, O VII) and low-excitation (O I, O II, O III) plasma components. The discrepancies pointed out by Juett et al. (2004) regarding the observed and measured positions for the Kα and Kβ lines in O I still stood. Gatuzz et al. (2013) report an oxygen abundance close to solar, which, in essence, dissents from the conclusions reached by Pinto et al. (2010, 2013).

Laboratory measurements of the O I K vacancy states (Caldwell et al. 1994; Krause 1994; Menzel et al. 1996; Stolte et al. 1997; McLaughlin et al. 2013), specifically the $1s2s^22p^5\ ^3P^o$ resonance, also show a bothersome scatter. This issue will be addressed more fully in Section 2.3.4 since this uncertainty, and that of the observations of interstellar oxygen X-ray spectra, are at the heart of the remaining issue of absolute energy normalization. The recent experiment of McLaughlin et al. (2013) is similar to the earlier study by Stolte et al. (1997), but the entire resonance region is now covered in one continuous scan in photon energy rather than the previous piecemeal scans for the lower $n = 2$ member and the higher $3 \leqslant n \rightarrow \infty$

Rydberg series; however, nearly identical energy positions are reported. The new theoretical results, on the other hand, are obtained from a 910-level *R*-matrix calculation that, upon close inspection, are essentially equivalent to those in Gorczyca & McLaughlin (2000). Thus, there is nothing substantively new learned from this study; it reconfirms the same resonance energy positions. This issue will be addressed more fully in Section 2.3.4.

The ultimate purpose of the present study is to arrive at a consensus for the best description of the photoionization cross section for neutral atomic oxygen. To this end, it is advantageous to create a single photoabsorption model that is transparent to all atomic data users. This is most easily accomplished by formulating an analytical expression that includes all the desired essential features: accurate background cross sections (the "shoulders"), line positions, widths, and oscillator strengths. We accomplish this by appealing to a combination of *R*-matrix computations, laboratory measurements, tabulated solid-state absorption data, independent-particle (IP) data, multi-configuration atomic structure calculations, and astronomically observed X-ray lines. Given a consistent photoabsorption cross section, we then plan to use the same atomic description in two different X-ray spectral modeling codes to render the ISM oxygen K features.

2. ANALYTICAL MODEL CROSS SECTION

We attempt to develop an analytical expression for the most reliable photoabsorption cross section possible. We begin with new *R*-matrix calculations, which are slight improvements over earlier results (Gorczyca & McLaughlin 2000) that were benchmarked favorably with experiment (Stolte et al. 1997). These results, together with experimental measurements, allow for the most accurate representation of the strong $1s \rightarrow np$ resonances below the K edge. At energies far below the K-edge region, where only outer-shell photoionization occurs, we use the formula of Verner et al. (1996), which is a simple fit to the IP results of Reilman & Manson (1979), and is found to be in excellent agreement with the present *R*-matrix results. At higher energies, a fit to the tabulated data of Henke et al. (1993) is used; these data are assessed to be the most accurate since important shake-up and shake-off processes are also accounted for (see Section 2.3.1). The resulting total photoabsorption cross section as a function of photon energy $E = h\nu$ is thus partitioned as

$$\sigma_{PA}(E) = \sigma_{2s,2p}(E) + \sigma_{1s}^{res}(E) + \sigma_{1s}^{direct}(E). \qquad (1)$$

To illustrate this demarcation, we plot several data sets of the photoabsorption cross section in Figure 1, where the three energy regions are all depicted. For energies below ≈520 eV, the cross section consists solely of the $\sigma_{2s,2p}(E)$ outer-shell photoionization contribution, whereas, just below the K-edge region, the strong $1s \rightarrow np$ resonance absorption profiles dominate. At higher energies, the cross section is essentially due to direct $1s \rightarrow \epsilon p$ photoionization and accompanying photoionization-excitation and double photoionization (which the present $1s$-photoionization *R*-matrix calculations do not include as discussed in Section 2.3.1). These three regions, and the precise theoretical modeling of each, are henceforth outlined.

2.1. Outer-shell Photoionization

For the outer-shell photoionization cross section, we have verified that the fit of Verner et al. (1996) is reliable, and their
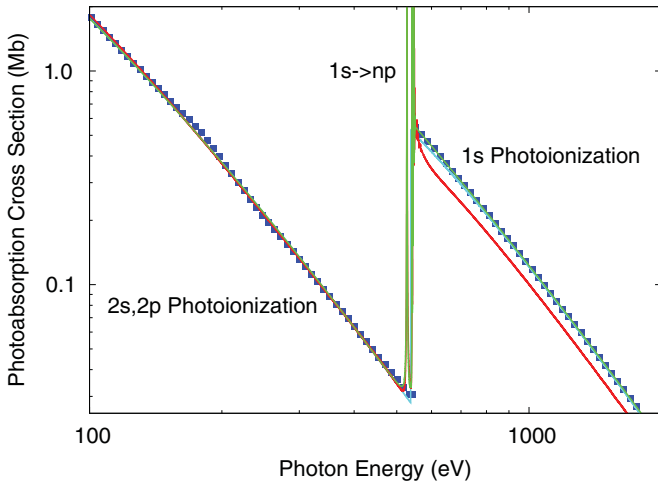
Figure 1. Broad view depiction of the O I photoabsorption cross section, indicating where the outer-shell ($\sigma_{2s,2p}$), inner-shell ($\sigma_{1s}^{\rm direct}$), and resonance ($\sigma_{1s}^{\rm res}$) contributions are most important. Shown are the present R-matrix (red curve), analytic formula (green curve), IP fit of Verner et al. (1996; cyan curve), and Henke et al. (1993) data (blue squares). The R-matrix results account for resonances but are missing two-electron contributions at higher energies (see text). The fit incorporates all the correct physics.

(A color version of this figure is available in the online journal.)

analytical formula

$$\sigma_{2s,2p}(E) = \sigma_0 \left[(x - 1)^2 + y_w^2\right] y^{(p-11)/2}\left(1 + \sqrt{y/y_a}\right)^{-p} \quad (2)$$

is therefore adopted, where $x = E/E_0 - y_0$, $y = \sqrt{x^2 + y_1^2}$, and the fitting parameters σ_0, E_0, y_a, p, y_w, y_0, and y_1 are listed in Table 1. The fit in Figure 1 is in close agreement with the present R-matrix results and with the tabulated data of Henke et al. (1993) at energies slightly above the $2s$ ionization threshold up through the region just below the $1s \rightarrow np$ resonances. At lower energies, important channel-coupling effects and prominent outer-shell resonance structure are found in the R-matrix results (and modeled somewhat more crudely in Henke et al. 1993). However, since we are not concerned with such low energies, the present fit is sufficient. Just below the resonance region at about 520 eV, there is coupling between the (open) $2s^{-1}\epsilon p$ and (closed) $1s^{-1}np$ channels that gives rise to a slight dip in the $2s$ R-matrix cross section (not observable on the scale of Figure 1) due to a transfer of oscillator strength (Dias et al. 1997; Hansen et al. 1999). This small dip over such a narrow energy region is ignored in the present final model.

2.2. Inner-shell (High-energy) Photoionization

We find that the data of Henke et al. (1993), above the $1s$ threshold, can be accurately fitted with the expression

$$\sigma_{1s}^{\rm Henke}(E) = \sigma_{\rm th} \left[1 + \alpha_1 \left(\frac{E_{\rm th}}{E}\right) + \alpha_2 \left(\frac{E_{\rm th}}{E}\right)^2\right] \left(\frac{E_{\rm th}}{E}\right)^3, (3)$$

where the fit threshold position is chosen to be $E_{\rm th} = 544.544$ eV, giving a threshold cross section of $\sigma_{\rm th} = 1.07$ Mb and parameters $\alpha_1 = -0.7227$ and $\alpha_2 = 0.2153$, which are needed for further fitting (see Table 1). We choose this functional form in our effort to derive an expression that matches continuously from below each of the two main O II thresholds, and, therefore, only the two parameters α_1 and α_2 are needed to get the correct shape of the above-threshold cross section.

Table 1
Summary of Fitting Parameters

Cross Section	Parameters
$\sigma_{2s,2p}$	$\sigma_0 = 1745.0$, $E_0 = 1.24$, $y_a = 3.784$, $p = 17.64$
	$y_w = 0.07589$, $y_0 = 8.698$, $y_1 = 0.1271$
$\sigma_{1s}^{\rm res}$	$f_0 = 0.132$, $f_{0,\infty}^1 = \frac{3}{5}f_0$, $f_{0,\infty}^2 = \frac{2}{5}f_0$
	$1s2s^2 2p^4(^4P)np$ **Series** $(i_s = 1)$
	$E_{\rm th}^1 = 544.54$ eV, $\Gamma^1 = 0.1348$ eV
	$\mu_2^1 = 1.11$, $\mu_3^1 = 0.77$, $\mu_n^1 = 0.75$ $(n \geqslant 4)$
	$f_{0,2}^1 = 0.867 f_{0,\infty}^1$, $f_{0,3}^1 = 0.93 f_{0,\infty}^1$, $f_{0,n}^1 = f_{0,\infty}^1$ $(n \geqslant 4)$
	$1s2s^2 2p^4(^2P)np$ **Series** $(i_s = 2)$
	$E_{\rm th}^2 = 549.32$ eV, $\Gamma^2 = 0.1235$ eV
	$\mu_3^2 = 0.84$, $\mu_n^2 = 0.80$ $(n \geqslant 4)$
	$f_{0,3}^2 = 1.02 f_{0,\infty}^2$, $f_{0,n}^2 = f_{0,\infty}^2$ $(n \geqslant 4)$
$\sigma_{1s}^{\rm direct}$	$\alpha_1 = -0.7227$, $\alpha_2 = 0.2153$

Note. The fitting data for each of the two series $i_s = 1$ and $i_s = 2$ follow the respective designations (bold faced).

2.3. Resonance Region

Our strategy in the $1s \rightarrow np$ resonance region is first to formulate an analytical fit (see Section 2.3.2) to the results from new R-matrix calculations (detailed in Section 2.3.1). The fit parameters are then adjusted slightly to match the experimental resonance positions and oscillator strengths, highlighting both the best assessment of the absolute energy scales as determined by line observations and the smooth consistent merging to the above-threshold cross section.

2.3.1. R-matrix Calculations

The present R-matrix approach is based closely on the earlier work of Gorczyca & McLaughlin (2000), the essential difference being in the present removal of pseudo-resonances. Further improvements include, first, a new computation of the spectator Auger widths using a resonance time-delay matrix analysis (Smith 1960) within an independent R-matrix calculation for the $e^- - $O II scattering. A second improvement involves a smooth turn-off of the spectator Auger damping $E \rightarrow E + i\Gamma/2$ (Gorczyca & Robicheaux 1999; Gorczyca & McLaughlin 2000) as the effective quantum number tends to the orbital angular momentum ($\nu \downarrow l$) to avoid the discontinuity previously seen when the quantum defect approach is abruptly turned off. Here, we allow the width to vanish continuously ($\Gamma \rightarrow 0$) in this limit before the quantum defect channel is omitted (Gorczyca & Badnell 2000).

As in earlier work (Gorczyca & McLaughlin 2000), we also emphasize the importance of accounting for orbital relaxation following inner-shell photoionization: the $2s_r$ and $2p_r$ "relaxed" orbitals in the final $1s2s_r^2 2p_r^4$ O II vacancy state differ significantly from those in the initial O I $1s^2 2s_g^2 2p_g^4$ ground state because of the doubling of the effective charge seen in the O II state. As a result, the computation of the direct cross section involves an overlap amplitude factor proportional to the $\langle 2s_g | 2s_r \rangle$ and $\langle 2p_g | 2p_r \rangle$ orbital overlap integrals; it is, therefore, imperative to account for this orbital difference. Within an orthonormal basis methodology, such as the R-matrix method we use here (Burke 2011; Berrington et al. 1995), the only way to account for the difference in orbitals is by introducing *pseudo-orbitals* (e.g., $\overline{3s}, \overline{3p}$) such that the relaxed excited state can be described in terms of the ground state and the pseudo-orbitals via

$$1s2s_r^2 2p_r^4 = c_1 1s2s_g^2 2p_g^4 + c_2 1s2s_g^2 2p_g^3\overline{3p}$$
$$+ c_3 1s2s_g 2p_g^4\overline{3s} + \dots . \quad (4)$$
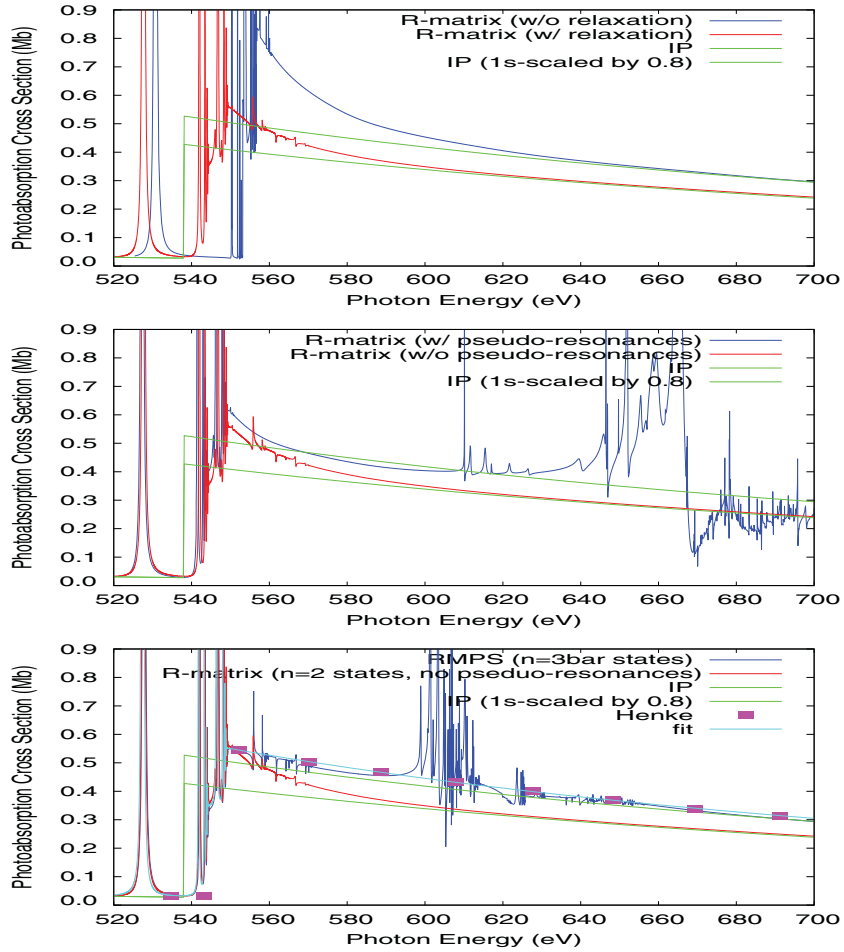
Figure 2. *R*-matrix photoabsorption cross sections computed with and without relaxation effects and/or pseudo-resonance elimination. The red curve shows the definitive *R*-matrix calculation, which includes relaxation effects via the use of pseudo-orbitals. The blue curve in the upper plot shows results without relaxation, indicating a gross overestimate of the threshold energy position and cross section. The blue curve in the middle plot shows the results when using pseudo-orbitals but not using the pseudo-resonance elimination method (Gorczyca et al. 1995), giving large, unphysical features that permeate the threshold region and below. The two green curves show the IP asymptote and that reduced by 80% due to relaxation effects. The blue curve in the lower plot shows the results when including the additional $1s2s^22p^3\overline{3p}$ and $1s2s2p^4\overline{3s}$ target pseudo-states to give an approximate representation of the photoionization-excitation and double-photoionization channels, while eliminating all additional pseudo-resonances that are not associated with these pseudo-channels.

(A color version of this figure is available in the online journal.)

This procedure takes care of the relaxation effect and, in the present case, the reduction factor can be independently computed from simple multi-configuration Hartree–Fock (MCHF) calculations (Froese Fischer 1991) of $|c_1|^2 = 0.80$. There is, thus, an analytically predicted reduction effect by a factor of 0.80 due to relaxation, and the remaining 20% of the oscillator strength goes into photoionization-excitation and double photoionization. A discussion of these various contributions is given in the early experimental study of Ne I photoionization by Wuilleumier & Krause (1974; see, especially, their Figure 8).

The effect of relaxation can also be seen by comparing the present *R*-matrix cross section with one where relaxation is not taken into account (Figure 2). The present, final *R*-matrix cross section asymptotically approaches the IP fit cross section of Verner et al. (1996), which is the scaled 1*s* cross section after the latter has had the 1*s* contribution multiplied by a factor of 0.80. This is the same overlap factor we compute from an independent MCHF calculation, thus independently confirming the 20% reduction effect. The original IP calculations (Reilman & Manson 1979), upon which Verner et al. (1996) based their fit, did not include relaxation effects. Consequently, their asymptotic value reflects the *total* photoabsorption cross section;

this total includes shake-up and shake-off processes in addition to the direct 1*s* photoionization (without secondary excitation or ionization).

However, as also seen in Figure 2, even though the unrelaxed orbital results approach the full IP cross section (Verner et al. 1996) asymptotically, they grossly overestimate the correct cross section just above the K-shell threshold; here, only the (relaxed) direct photoionization is energetically allowed. This overvalue is carried below threshold, leading to an unphysically enhanced resonance-oscillator strength. Moreover, the threshold energy *position* is also overestimated—by more than 10 eV—because of the inaccurate representation of the $1s2s^22p^4$ inner-shell vacancy state.

It is, therefore, critical to account for relaxation effects; this is accomplished in the present theoretical methodology by including additional pseudo-orbitals in the atomic orbital basis set. However, without proper care, this procedure can lead to spurious *pseudo-resonance* structure (Gorczyca et al. 1995), as is also shown in Figure 2. The present *R*-matrix results, which were computed with pseudo-orbitals and with a proper elimination of pseudo-resonances (Gorczyca et al. 1995), are compared with similar *R*-matrix results without such an
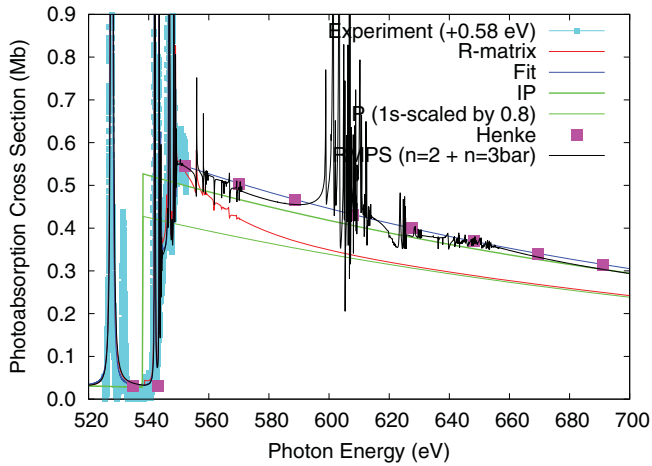
Figure 3. Near- and above-threshold cross section: the red curve and black curve show the definitive *R*-matrix and RMPS calculations, respectively. The two green curves show the IP asymptote and that reduced by 80% due to relaxation effects. The final fit formula is shown as the blue curve; the experimental results of Stolte et al. (1997), shifted by +0.58 eV, are given as the cyan data points; and the solid-state results of Henke et al. (1993) are given as the magenta squares.

(A color version of this figure is available in the online journal.)

elimination. It is seen that the latter cross section exhibits large, spurious pseudo-resonance structure at higher energies. Further, these broad, unphysical resonance features permeate even down to the threshold region, resulting in an overestimate of the near-threshold cross section (and the resonance absorption oscillator strengths below threshold). By applying the pseudo-resonance elimination method (Gorczyca et al. 1995), the cross section becomes smooth throughout, and provides the most reliable resonance oscillator strengths as discussed in Section 2.3.1. The earlier *R*-matrix calculations did not use a pseudo-resonance elimination method and, therefore, overestimated the resonance absorption oscillator strengths (see Gorczyca & McLaughlin (2000) and their Figure 2).

We can improve the asymptotic situation somewhat by including the orthogonal compliments to the $1s2s^22p^4$ O$^+$ (relaxed) target states, namely the additional *pseudo-states* that are composed of the $1s2s^22p^3\overline{3p}$ and $1s2s2p^4\overline{3s}$ configurations (with smaller $\approx$20% mixing of the $1s2s^22p^4$ configurations). This *R*-matrix with pseudo-states (RMPS) method (Burke 2011), as implemented in the present codes following the developments of Gorczyca & Badnell (1997), gives a somewhat crude, approximate description of the photoionization-excitation and double-photoionization channels, and, importantly, leads to the correct high-energy photoionization asymptote, as seen in the lower panel of Figure 2. The implementation of *R*-matrix methods on modern, massively parallel machines (Ballance & Griffin 2006) will allow for a much larger, converged RMPS treatment of the problem.

The findings thus far regarding the above-threshold cross section are summarized in Figure 3: Asymptotically, the present *R*-matrix cross section approaches the IP results after the (dominant) $1s$ contribution has been scaled by a factor of 0.8 to account for relaxation, whereas the RMPS values show the correct asymptote but are still plagued by pseudo-resonances. The fit of Verner et al. (1996) at threshold is an extrapolation of the high-energy IP cross section of Reilman & Manson (1979), and, therefore, does not include the correct threshold rise as is seen in the *R*-matrix results. On the other hand, the data of Henke et al. (1993), which are based on solid-state measurements, show the correct threshold and asymptotic cross sections and are

devoid of pseudo-resonance structure; therefore, we choose this continuous data as the best representation of the cross section for energies above threshold. The *R*-matrix and RMPS cross sections just above threshold coincide with the data by Henke et al. (1993). Lastly, the measurements of Stolte et al. (1997) are consistent with the *R*-matrix results throughout, as we address in Section 2.3.6.

2.3.2. Analytical Fit to the $1s \rightarrow np$ Resonance Region

The formula to fit the single-resonance photoabsorption cross section—parameterized by an absorption oscillator strength f, a resonance position E_r, and a width Γ—is given by (see Bethe & Salpeter 1957, Equation (71.19))

$$\sigma_{\mathrm{PA}}(E) = \frac{\pi(k_e e^2)h}{mc}\frac{df}{dE}, \qquad (5)$$

where the oscillator strength per unit energy for an isolated resonance takes the form

$$\frac{df}{dE} = f\frac{\Gamma/2\pi}{(E-E_r)^2 + (\Gamma/2)^2}; \qquad (6)$$

i.e., it is equal to the discrete oscillator strength f times an energy-normalized Lorentzian,

$$\int dE \frac{\Gamma/2\pi}{(E-E_r)^2 + (\Gamma/2)^2} = 1. \qquad (7)$$

Therefore, the photoabsorption profile can be characterized as

$$\sigma_{\mathrm{PA}}(E) = \beta f\frac{\Gamma/2\pi}{(E-E_r)^2 + (\Gamma/2)^2}, \qquad (8)$$

with

$$\beta = \frac{\pi k_e e^2 h}{mc} = 109.7626\,\mathrm{Mb\,eV}.$$

For an entire Rydberg series—characterized for each member by a principal quantum number n, resonance positions E_n, width Γ (n-independent for inner-shell spectator Auger decay), and the oscillator strengths f_n—can be parameterized by a quantum defect μ, a threshold energy E_{th}, and an n-independent "strength" f_0:

$$E_n \approx E_{\mathrm{th}} - \frac{Z^2 E_{\mathrm{au}}}{2(n-\mu)^2},$$

$$f_n \approx \frac{f_0}{(n-\mu)^3}, \qquad (9)$$

where $E_{\mathrm{au}} = 27.211\,\mathrm{eV}$. This discrete expression carries over to an analytic above-threshold cross section

$$\lim_{E \downarrow E_{\mathrm{th}}} \sigma_{\mathrm{PA}}(E) = \beta\frac{f_0}{Z^2 E_{\mathrm{au}}}, \qquad (10)$$

which must be considered when developing a consistent, continuous formulation through threshold.

Equation (9), based on quantum defect theoretical considerations, is precise in the limit $n \rightarrow \infty$, but deficient for the lower resonances ($n = 2, 3$). The lowest members are more appropriately modeled by using separate (energy-dependent) quantum defects and oscillator strengths.

For multiple Rydberg series, if the interaction between them is neglected, the contribution from each series can be considered separately. We apply this approach to the two dominant photoabsorption series in oxygen, namely $1s2s^22p^4(^4P)np$ and $1s2s^22p^4(^2P)np$ (labeled, respectively, by the indices $i_s = 1$ and $i_s = 2$), giving a two-series resonance cross section parameterized as

$$\sigma_{1s}^{\text{res}}(E) = \beta \sum_{i_s=1}^{2} \left[\sum_{n=n_{\min}=i_s+1}^{\infty} \frac{f_{0,n}^{i_s}}{(n-\mu_n)^3} \right.$$
$$\times \frac{\Gamma_n^{i_s}/2\pi}{\left(E - (E_{\text{th}}^{i_s} + Z^2 E_{\text{au}}/(n-\mu_n)^2)\right)^2 + \left(\Gamma_n^{i_s}/2\right)^2}$$
$$\left. + \frac{f_{0,\infty}^{i_s}}{Z^2 E_{\text{au}}} \left(\frac{1}{2} - \frac{1}{\pi} \arctan\left(\frac{E_{\text{th}}^{i_s} - E}{\Gamma/2} \right) \right) \right]. \quad (11)$$

The last term ensures that, since the below-threshold contribution has effectively been Auger broadened, i.e., convoluted with a Lorentzian of width Γ within each resonance energy interval $\Delta E \sim E_{\text{au}}/(n-\mu)^3$, the step function, due to the above-threshold continuum photoionization, is likewise convoluted near threshold:

$$\sigma(E \approx E_{\text{th}}) = \int_{-\infty}^{\infty} dE' \frac{\Gamma/2\pi}{(E - E')^2 + (\Gamma/2)^2}$$
$$\times \left[\frac{f_{0,\infty}}{Z^2 E_{\text{au}}} \theta(E - E_{\text{th}}) \right], \quad (12)$$

where $\theta(E - E_{\text{th}})$ denotes the Heaviside step function at threshold. As the energy is increased above threshold, this expression is continuously extended to have the correct asymptotic tail as determined from our fit to the Henke et al. (1993) data in Equation (3), taking instead the form above threshold

$$\sigma_{1s}^{\text{direct}}(E) = \beta \sum_{i_s=1}^{2} \frac{f_{0,\infty}^{i_s}}{Z^2 E_{\text{au}}} \left[\frac{1}{2} - \frac{1}{\pi} \arctan\left(\frac{E_{\text{th}}^{i_s} - E}{\Gamma/2} \right) \right]$$
$$\times \frac{\left[1 + \alpha_1 \left(\frac{E_{\text{th}}^{i_s}}{E} \right) + \alpha_2 \left(\frac{E_{\text{th}}^{i_s}}{E} \right)^2 \right]}{[1 + \alpha_1 + \alpha_2]} \left(\frac{E_{\text{th}}^{i_s}}{E} \right)^3. \quad (13)$$

In our R-matrix calculations, the oscillator strength (cross section) is found to be partitioned into the two dominant series by the fractions of 3/5 and 2/5 for the $1s2s^22p^4(^4P)np$ and $1s2s^22p^4(^2P)np$ series, respectively, instead of the statistical weighting of 2/3 and 1/3, because of channel coupling in the threshold region. As a result, the net oscillator strength density above threshold, which we find to be $f_{0,\infty} = 0.132$, is partitioned as $f_{0,\infty}^1 = 0.6 f_{0,\infty}$ and $f_{0,\infty}^2 = 0.4 f_{0,\infty}$.

Our strategy is, first, to fit this expression to our present R-matrix results to get a good representation of the oscillator strengths and quantum defects, using the threshold energies and widths from the R-matrix runs. Then, the threshold energies are slightly adjusted and the analytical (Lorentzian) fit is further convoluted with the experimental (Gaussian) width to obtain a good fit to the experimental resonance spectrum. Before fitting this expression to our current results, we address resonance energy positions.

2.3.3. Resonance Energy Positions from Astronomical Observations

Oxygen K-shell photoabsorption in the ISM has been observed with both the *Chandra* and *XMM-Newton* satellite-borne

Table 2
Chandra Observations Used in This Work

Source	ObsID	Date	Exposure (ks)	Read Mode
4U 1636−53	105	1999 Oct 20	29	TE
	1939	2001 Mar 28	27	TE
	6636	2007 Jul 2	26	CC
	6635	2006 Mar 22	23	CC
4U 1735−44	704	2006 Jun 9	24	TE
	6637	2006 Aug 17	25	CC
	6638	2007 Mar 15	23	CC
4U 1820−30	1021	2001 Jul 21	9.6	TE
	1022	2001 Sep 12	11	TE
	6633	2006 Aug 12	25	CC
	7032	2006 Nov 5	47	CC
	6634	2010 Oct 20	26	CC
Cygnus X-1	3407	2001 Oct 28	17	CC
	3724	2002 Jul 30	8.8	CC
Cygnus X-2	1102	2003 Sep 23	28	TE
	8599	2007 Aug 23	59	CC
	8170	2007 Aug 25	65	CC
	10881	2009 May 12	66	CC
GX 9+9	703	2000 Aug 22	20	TE
	11072	2010 Jul 13	95	TE
XTE J1817−330	6615	2006 Feb 13	18	CC
	6616	2006 Feb 24	29	CC
	6617	2006 Mar 15	47	CC
	6618	2006 May 22	51	CC

Note. TE: TIMED; CC: CONTINUOUS.

observatories. The High Energy Transmission Grating Spectrometer (HETGS) of *Chandra*, in combination with the Advanced CCD Imaging Spectrometer (ACIS), may provide the best spectral resolution with adequate sensitivity. It is exemplified by the Juett et al. (2004) study, using the medium energy gratings (resolving power of 0.023 Å FWHM and an absolute wavelength accuracy of 0.011 Å; Canizares et al. 2005) the HETGS to observe six Galactic X-ray sources. For the present work, we carry out a reanalysis of these observations in an attempt to improve the positions of the O I Kα ($1s \rightarrow 2p$) and Kβ ($1s - 3p$) resonances. The XTE J1817−330 source, previously treated by Gatuzz et al. (2013), is included as well as some additional spectra for the sources considered by Juett et al. (2004).

Observational specifications for the seven low-mass X-ray binaries used in this analysis are listed in Table 2. The observations were taken in continuous clocking (CC) mode or time exposure (TE) mode. In CC mode, the temporal resolution is increased to minimize the pileup effect (Cackett et al. 2008). In TE mode, the ACIS instrument periodically reads the collected photons. All the spectrum files, response files, auxiliary response files, and background files were taken from the *Chandra* Grating-Data Archive and Catalog TGCat.[11] We use the ISIS[12] package (version 1.6.2-18) for spectral fitting.

We fitted all the observations for each source simultaneously using a simple `powerlaw+gaussians` model in the oxygen-edge region (21–24 Å). The power-law parameters were taken as independent, free parameters for each observation. We apply cash statistics because of the low signal-to-noise ratio in these spectra, which requires a minimal grouping of the spectra of

[11] http://tgcat.mit.edu/.
[12] http://space.mit.edu/cxc/isis/.

Table 3
O I Kα and Kβ Line Positions (Å)

Source	Kα ($1s - 2p$)		Kβ ($1s - 3p$)	
	Present	Juett et al. (2004)	Present	Juett et al. (2004)
4U 1636−53	$23.509^{+0.006}_{-0.004}$	23.507 ± 0.011	$22.889^{+0.005}_{-0.004}$	22.915 ± 0.013
4U 1735−44	23.507 ± 0.009	23.503 ± 0.009	$22.890^{+0.009}_{-0.006}$	22.861 ± 0.006
4U 1820−30	23.509 ± 0.004	23.514 ± 0.010	$22.880^{+0.009}_{-0.010}$	22.867 ± 0.015
Cygnus X-1	$23.507^{+0.003}_{-0.004}$	23.511 ± 0.007	$22.882^{+0.011}_{-0.009}$	$22.888^{+0.023}_{-0.016}$
Cygnus X-2	23.508 ± 0.002	23.508 ± 0.004	$22.883^{+0.010}_{-0.006}$	$22.877^{+0.028}_{-0.026}$
GX 9+9	$23.505^{+0.006}_{-0.004}$	23.517 ± 0.009	$22.900^{+0.008}_{-0.010}$	22.906 ± 0.018
Mean position[a]	23.507 ± 0.005	23.510 ± 0.008	22.886 ± 0.008	$22.885^{+0.017}_{-0.015}$
XTE J1817−330	23.506 ± 0.001		22.889 ± 0.004	
Mean position[b]	23.507 ± 0.004	23.510 ± 0.008	$22.887^{+0.008}_{-0.007}$	$22.885^{+0.017}_{-0.015}$

Notes.
[a] Excluding XTE J1817−330.
[b] Including XTE J1817−330.

at least one count per spectral bin (see Humphrey et al. 2009; Baldi et al. 2012). Table 3 shows the O I Kα and Kβ absorption line positions obtained from these fits. First, we list the mean position values excluding XTE J1817−330 to compare with those originally reported by Juett et al. (2004). When this source is taken into account, there is a slight decrease of the mean-value error bars. In the case of Cygnus X-1, the values in Juett et al. (2004) correspond to the average of ObsID 3407 and ObsID 3742. From the confidence intervals, it may be appreciated that the present results are in agreement with the line positions estimated by Juett et al. (2004), but with improved statistics.

The transition energy of the O I Kα ($1s \rightarrow 2p$) line is also estimated using the well-exposed *XMM-Newton* RGS spectrum of Mrk 421 (Kaastra et al. 2006). This spectrum shows strong interstellar Kα absorption lines from O I at 23.5138 ± 0.0022 Å and O VII at 21.6027 ± 0.0021 Å. Since accurate theoretical values (Drake 1988; Cann & Thakkar 1992) and high-precision laboratory measurements (Engstrom & Litzen 1995) have been reported for the latter at 21.6015 Å and 21.60195 ± 0.0003 Å, respectively, we assume a small offset on the wavelength scale for this data set of 0.8 mÅ, which is well within the systematic uncertainty of the RGS. Correcting for this small difference (and assuming that the O VII line shows no intrinsic redshift), we find an energy of 527.30 ± 0.05 eV for the O I Kα line. In summary, a list of the O I $1s \rightarrow 2p$ and $1s \rightarrow 3p$ line energies deduced from astronomical observations is given in Table 4. The listed *Chandra* line energies, unlike the *XMM-Newton*, were neither re-scaled with the O VII Kα line nor Doppler corrected for the motion of the Earth around the Sun. Regarding the former issue, Gatuzz et al. (2013) quotes a line energy of 21.593 ± 0.002 Å for the *Chandra* observation of O VII Kα toward XTE J1817−330, which is 9 mÅ short of the laboratory standard. If the wavelength scale is adjusted accordingly, our *Chandra* O I Kα position in Table 4 would be reduced to 527.26 ± 0.09 eV, and would be in better agreement with the *XMM-Newton* value.

Recently, Liao et al. (2013) conducted a new and independent investigation of 36 *Chandra* HETG observations of 11 low-mass X-ray binaries, which accounts for the Galactic rotation velocity relative to the rest frame and uses a similar merging of corrected spectra. They use a Bayesian analysis to quantify systematic uncertainties and bias corrections, obtaining a resonance position with improved statistics. The resulting energy position of

527.39 ± 0.02 eV, as listed in Table 4, is in agreement with our average observed value of 527.37 eV.

2.3.4. Resonance Energy Positions from Laboratory Measurements

We now consider the laboratory data for atomic oxygen. In Figure 4, we show the differences between the measured resonance energies for two experiments, namely Menzel et al. (1996) and Stolte et al. (1997). First, there is a systematic, almost linear change of the energy differences. This may be attributed to small remaining calibration uncertainties in at least one of the two datasets. Further, from the scatter, it is seen that the correlation between both datasets is much better than suggested by the formal error bars. This is probably because the error bars include a systematic uncertainty that may be nearly the same for all transitions. From a linear regression, we obtain for this energy difference (in eV units): $\Delta E = (36.357 \pm 0.010) - (0.0670 \pm 0.0016)E$, with a scatter of 0.03 eV (much smaller than the nominal uncertainties of 0.10 eV). Next, we compare the measurements of Krause (1994) and Caldwell et al. (1994) with those of Stolte et al. (1997). In this case, we find no significant slope (best fit 0.0029 ± 0.0037) and only a constant offset of 0.444 ± 0.028 eV. We conclude that the relative energy scales of Krause (1994), Caldwell et al. (1994), and Stolte et al. (1997) agree, and that, most likely, the energy scale of Menzel et al. (1996) is slightly off. All these datasets, however, show a different offset for their absolute energy scale.

2.3.5. Resonance Energy Positions from Large MCHF Calculations

The *R*-matrix calculations seek to span an indenumerably infinite number of bound, autoionizing, and continuum states of O I within a single, orthonormal basis of configurations and orbitals. It therefore becomes difficult to describe any specific state to a high degree of accuracy. In the present calculation, we are limited to an active space of up to $n = 2$ physical orbitals and $\bar{n} = 3$ pseudo-orbitals. However, because the dominant $1s \rightarrow 2p$ transition energy is the source of a rather large ($\approx$0.5–0.6 eV) discrepancy between observations and laboratory experiments, we can shed further light on the issue by appealing to separate, highly correlated theoretical calculations for the initial and final states. To this end, we use the sophisticated MCHF atomic structure package (Froese Fischer 1991) to perform a series of calculations using separate, large configuration-interaction (CI)

Table 4
Line Energies (eV) for O I

Data Set	$1s \rightarrow 2p$	$1s \rightarrow 3p$	ΔE
Astronomical observations			
Chandra, average of seven sources	527.44 ± 0.09	541.72 ± 0.18	14.28 ± 0.21
XMM-Newton, Mrk 421	527.30 ± 0.05	541.95 ± 0.28	14.65 ± 0.33
Juett et al. (2004), six sources	527.41 ± 0.18	541.77 ± 0.40	14.36 ± 0.58
Average	**527.37**		
Chandra, Liao et al. (2013)	527.39 ± 0.02		
Laboratory measurements			
McLaughlin et al. (2013)	526.79 ± 0.04	541.19 ± 0.04	14.40 ± 0.08
Stolte et al. (1997)	526.79 ± 0.04	541.20 ± 0.04	14.41 ± 0.08
Krause (1994), and Caldwell et al. (1994)	527.20 ± 0.30		
Menzel et al. (1996)	527.85 ± 0.10	541.27 ± 0.15	13.41 ± 0.25
MCHF calculations			
($n_{max} = 6$)	527.49		

Note. The average of the *Chandra* and *XMM* data is found to be 527.37 eV and is indicated in bold.

Table 5
MCHF Data for $1s^2 2s^2 2p^4 (^3P) \rightarrow 1s 2s^2 2p^5 (^3P)$ in O I

n_{max}	E_i (a.u.)	E_f (a.u.)	ΔE (eV)	f_L	f_V
2	-74.85830	-55.44337	528.29	0.133	0.121
3	-74.99720	-55.63645	526.82	0.107	0.102
4	-75.06477	-55.68599	527.31	0.098	0.101
5	-75.08774	-55.70510	527.41	0.093	0.097
6	-75.09707	-55.71152	527.49	0.097	0.096

Notes. Results are given as a function of n_{max}, the maximum principal quantum number included in the active space expansion of configurations obtained by single and double promotions out of the initial or final configuration. Separate orbital bases are used for initial and final states, and relativistic corrections account for an additional ≈ 0.03 eV to the transition energy. f_L and f_V are, respectively, the oscillator strengths in the length and velocity gauges.

expansions, thus increasing the basis size to study the convergence of transition energies and oscillator strengths. Specifically, starting with the initial $1s^2 2s^2 2p^4 (^3P)$ configuration, we use a basis consisting of all configurations obtainable by any single or double promotions from the outer $n = 2$ orbitals into the active set of orbitals. For $n_{max} = 2$, the additional $1s^2 2s 2p^5$ and $1s^2 2p^6$ configurations are taken into account; for $n_{max} = 3$, configurations such as $1s^2 2s^2 2p^3 3\ell$, $1s^2 2s 2p^4 3\ell$, $1s^2 2s^2 2p^3 3\ell 3\ell'$, $1s^2 2s 2p^3 3\ell 3\ell'$, and $1s^2 2p^3 3\ell 3\ell'$ ($3\ell = \{3s, 3p, 3d\}$) are also included. This procedure is repeated for $n_{max} = 4, 5, 6$, and, at each stage, a full-scale MCHF calculation is performed, optimizing each of the separate orbitals from $n = 1$ to $n = n_{max}$ to produce a lengthy multi-configuration wavefunction for the initial state. This same procedure is repeated for the final state, re-optimizing all of the orbitals separately. Last, for given initial and final wavefunctions (using completely different, non-orthogonal orbital bases), the absolute energies, transition energies, and oscillator strengths are computed. The results, listed in Table 5, show that the transition energy oscillates significantly between the observed and experimental values at first, but converges to a value consistent with that determined from the X-ray observations.

2.3.6. Final Resonance Fit

By fitting the expression in Equation (11) to the R-matrix results, we obtain the parameters that are listed in Table 1. However, our initial fit used, in addition to the same widths as

determined in the R-matrix run (0.1348 eV and 0.1235 eV for series $i_s = 1$ and $i_s = 2$, respectively), the theoretical threshold energy positions $E_{th}^1 = 544.74$ eV and $E_{th}^2 = 549.67$ eV. As is seen at all levels in Figure 5, this prescription provides an excellent fit to the R-matrix results. The fit formula was next compared with the experimental cross section of Stolte et al. (1997) (shifted by $+0.58$ eV to position the $1s \rightarrow 2p$ resonance at 527.37 eV). However, to align our fit with these shifted experimental results, which comprise our assessment of the most accurate resonance positions, we had to shift our theoretical threshold energies by -0.2 eV and -0.35 eV for the two series $i_s = 1$ and $i_s = 2$, respectively. This has the simple effect of shifting each resonance of each series by these amounts. Further, to obtain the most meaningful comparison, it was necessary to convolute the fitting expression with a Gaussian of 182 meV FWHM to simulate the experimental resolution. Finally, it was necessary to upscale the $n = 2$ oscillator strength to match the more reliable MCHF value of 0.097 (see Table 5); the R-matrix $n = 2$ oscillator strength was scaled down by a factor of 0.80 from the $n \rightarrow \infty$ series limit; and we use, as the final fit, the slightly increased value $f_{0,2}^1 = 0.867 f_{0,\infty}^1$, which ensures an oscillator strength of $f = f_{0,2}^1 / (2 - \mu_2^1)^3 = 0.097$.

With these final adjustments, the resulting fit reproduces the experimental results well, except for the $n = 2$ resonance strength. In particular, the quantum defects for each of the two series, as determined from the fit to the R-matrix results, align satisfactorily with the experimental values indicating that, regarding energy determination, the main source of error lies in determining accurate threshold positions. Further, with respect to the experimental spectrum, it seems that, if there is any error, it must be an overall global offset that we assume here to be -0.58 eV. The fit formula of Equation (11) could have just been modified by replacing the unit Lorentzian profiles by unit Voigt profiles, but it is more straightforward to simply convolute the resulting cross section numerically. Nevertheless, this highlights the flexibility of the analytical fitting formula in that the particular resonance shape can be, if desired, easily accounted for analytically.

Finally, the experiment has a noticeable signal due to molecular O_2 contamination in the beam as evidenced by the strong $1s \rightarrow \pi^*$ resonance at 531 eV. Consequently, there is an additional signal in the experiment throughout the K-edge region, and the experimental procedure does not provide the most
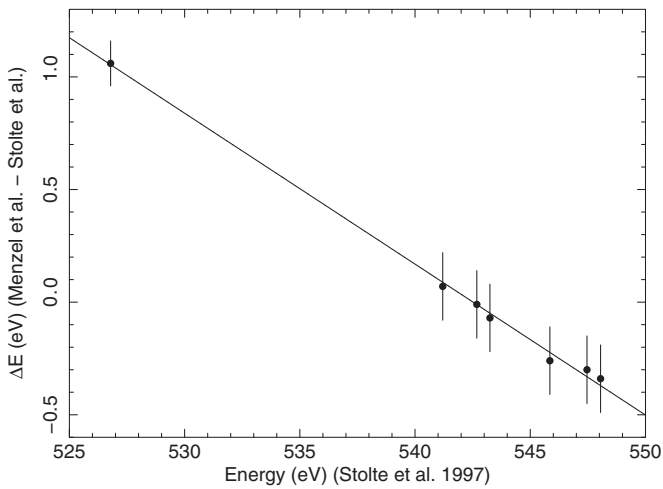
Figure 4. Comparison between the experimental resonance positions of Menzel et al. (1996) and Stolte et al. (1997).

accurate benchmark away from resonance. On resonance, the signal is so strong and predominantly atomic in nature that the small molecular admixture would not affect the oscillator strength as much.

3. COMPARISON WITH OTHER MODELS

The three datasets of X-ray absorption currently used in spectral modeling codes we compare with the present fit are: (1) the *R*-matrix cross sections of Gorczyca & McLaughlin (2000); (2) the XSTAR modeling code, which uses the *R*-matrix cross sections of García et al. (2005) except for independent data for the lowest $1s \rightarrow 2p$ resonance; and (3) SPEX, which is based on calculations with HFR (Cowan 1981) for resonances and data by Verner et al. (1996) elsewhere. A comparison is given in Figure 6 between these various approaches and the present fit, where several points must be brought to light. First, the cross section of Gorczyca & McLaughlin (2000), at least with respect to resonance positions, is close to the present fit since it is based on similar *R*-matrix calculations. However, the resonance oscillator strengths and the above-threshold cross section are higher, which we explain in Section 2.3.1 as being due to pseudo-resonance contamination present in the earlier *R*-matrix calculations. Further, the earlier *R*-matrix results show a minor discontinuity at the low-energy tail of the $1s2s^2 2p^4 (^4P)3p$ resonance ($E \approx 538$ eV) because of the sudden turn off of spectator Auger damping, which, as discussed in Section 2.3.1, we alleviate in the present study.

The *R*-matrix results in XSTAR by García et al. (2005) are seen in Figure 6 to be even higher than the present fit, regarding both the resonance oscillator strengths and the above-threshold cross section, and this is believed to be due to an insufficient treatment of both CI and relaxation effects. In García et al. (2005), relaxation is partially accounted for by optimizing the orbitals on a weighted sum of closed $1s$-shell and $1s$-vacancy states of O II. Last, the SPEX model has gaps in the total oscillator strength density since only a finite number of terms are included for each Rydberg series. The unconvoluted natural widths are underestimated (in the original data, at least) since the spectator Auger decay was not taken into account; the included participator Auger width approaches zero as n increases ($\Gamma_n^p \sim n^{-3}$). Additionally, the above-threshold cross section is matched to the IP results of Verner et al. (1996), which, as discussed in Section 2.3.1, underestimate the threshold value.
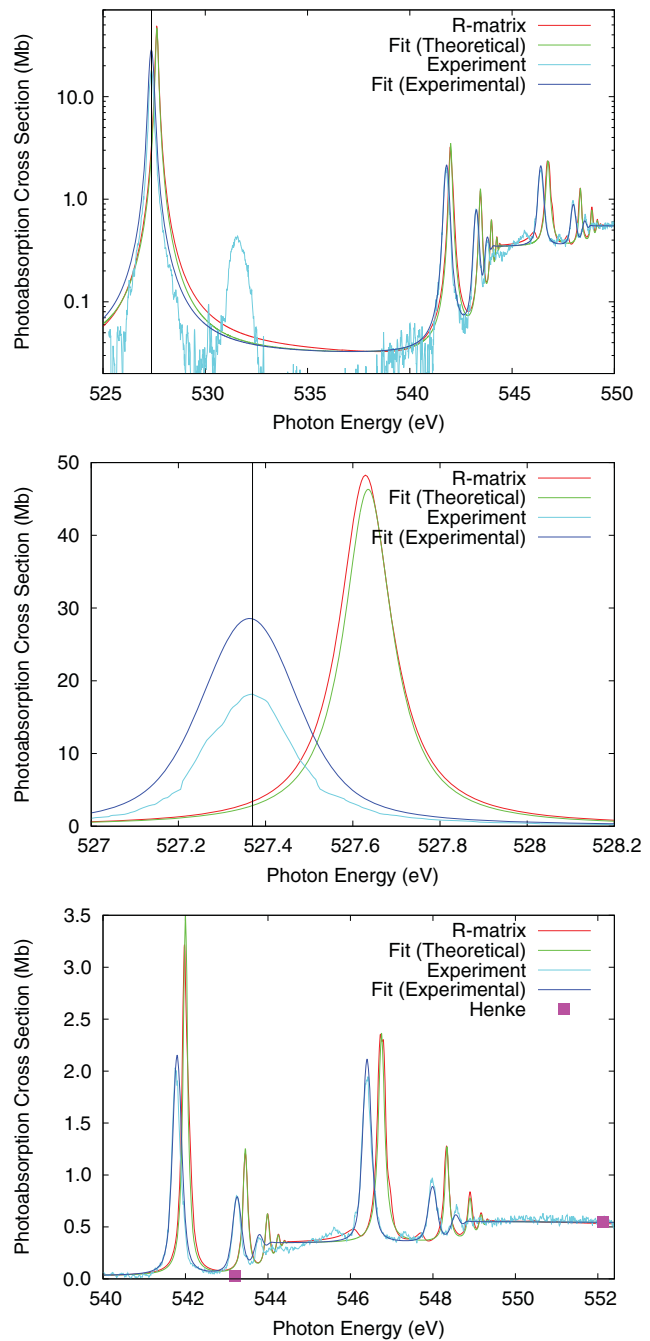
Figure 5. Fitting comparison: *R*-matrix results (red curve), analytical fit formula to theoretical results (green curve), experimental results of Stolte et al. (1997), shifted by +0.58 eV (cyan data points), analytical fit formula using adjusted threshold energies and convoluted with the experimental resolution of 182 meV (cyan curve), Henke et al. (1993) data (magenta squares), $1s \rightarrow 2p$ resonance position of 527.37 eV determined from observation (black vertical line, see text).
(A color version of this figure is available in the online journal.)

We also show the newer *R*-matrix results of McLaughlin et al. (2013), which are seen to closely reproduce the earlier *R*-matrix results of Gorczyca & McLaughlin (2000), including the overestimate of the above-threshold cross section, as discussed in Section 2.3.1. One additional shortcoming in the new *R*-matrix results is that, since spectator Auger decay is not implicitly accounted for in that formulation, the predicted natural widths are underestimated (and, indeed, scale unphysically as $1/n^3$ as $n \rightarrow \infty$).
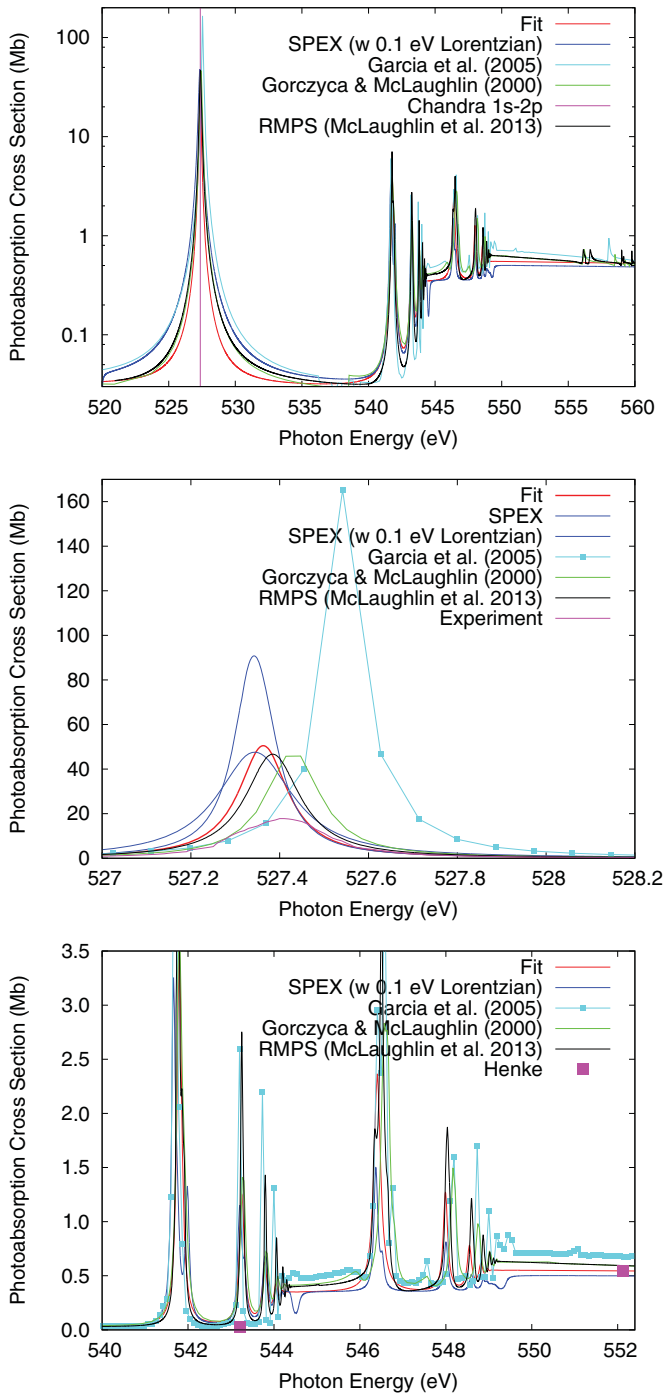
Figure 6. Comparison between various datasets: the present fit model (red curve), SPEX (blue curve), *R*-matrix results of García et al. (2005; cyan curve), *R*-matrix results of Gorczyca & McLaughlin (2000; green curve), *R*-matrix results of McLaughlin et al. (2013; black curve), Henke et al. (1993) data (magenta squares), and present *Chandra* position of the $1s \rightarrow 2p$ resonance at 527.37 eV (magenta vertical line). The earlier *R*-matrix results of Gorczyca & McLaughlin (2000) and the more recent *R*-matrix results of McLaughlin et al. (2013) are indistinguishable, except for the lowest $1s \rightarrow 2p$ resonance in the middle figure.

(A color version of this figure is available in the online journal.)

4. SUMMARY OF FITTING FORMULA

The final expression for the photoabsorption cross section consists of the sum of the cross sections in Equation (1), where $\sigma_{2s,2p}(E)$, $\sigma_{1s}^{\text{res}}(E)$ and $\sigma_{1s}^{\text{direct}}(E)$ are given by Equations (2), (11), and (13), respectively, and the required fitting parameters are

listed in Table 1. This final expression has several desirable features:

1. It is an analytical formula easily transportable between different platforms and modeling codes; the Fortran routine used to generate a numerical photoabsorption cross section for all energies involves only about 100 lines of code.
2. The formulation contains adjustable fitting parameters to best represent: (1) the K-edge positions; (2) the $n \rightarrow \infty$ energy-independent quantum defects and oscillator strengths; and (3) the energy-dependent quantum defects and oscillator strengths for the lower two resonances. From this fit, all relevant atomic parameters can be read off; for instance, the strongest $1s \rightarrow 2p$ oscillator strength can be computed from our fit as

$$f = f_{0,2}^1/(2 - \mu_2^1)^3 = 0.097,$$

and the integrated resonance strength is therefore given by $\beta f = 10.65$ Mb eV. Further modifications to these parameters can be made if so desired.
3. The energy spectrum is optimized on the resonance positions determined from a combined experimental and observational assessment.
4. A constant-resonance-width cross section—a Lorentzian profile that is predicted on physical grounds due to spectator Auger broadening—is implicitly included in the final expression, and can be further modified analytically to include additional broadening effects.
5. A consistent threshold formulation is obtained in that the $\lim_{n \rightarrow \infty} f_n$ for the (scaled) oscillator strength joins analytically and smoothly with the above-threshold oscillator strength density df/dE.
6. The consistent above-threshold cross section has the important factor of 0.80 reduction due to relaxation effects, and is then extended to higher energies to include the shake-up and shake-off processes. This results in photoionization-excitation and double-photoionization contributions to account for the 20% difference, giving the correct $E \rightarrow \infty$ high-energy asymptote, i.e., an accurate "shoulder."

5. CONCLUSION

We have developed an analytical expression that encapsulates all of the important physics in X-ray absorption of atomic oxygen at all photon energies relevant to spectral modeling. For energies below or above the K-edge resonance region, we use simple parametric fits to our best assessment of the cross section based on a convergence between experimental and theoretical data. The strong $1s \rightarrow np$ resonances belonging to the two dipole-favored Rydberg series, on the other hand, require special attention regarding the oscillator strengths (and analytic continuation to the above-threshold direct $1s$ cross section) and resonance positions. For this important region, we appeal to a combination of *R*-matrix and MCHF theoretical calculations, laboratory experiments, and X-ray astronomical observations. An outstanding issue is the large discrepancy of ≈ 0.6 eV between several recent observational assessments and the latest laboratory experiments. Unconventionally, we choose to use the final calibration as suggested by the observations, since several sources and an independent large MCHF calculation tend to add credibility to this choice. Further, the recent laboratory experiments (Stolte et al. 1997; McLaughlin et al. 2013) calibrated

the photon energy scale using the molecular oxygen Rydberg resonance features, and it is unclear to us how accurately those *molecular* positions are known, especially considering the uncertainties we find in the *atomic* resonance positions. A repeat of those experimental measurements, calibrated instead to the more well-known CO and CO_2 K-edge features, will be performed in the near future (W. C. Stolte 2013, private communication), which will shed more light on the existing discrepancy.

The ultimate goal of the present work is to establish a definitive, transparent, and portable photoabsorption cross section that can be incorporated in the two spectral modeling codes, namely XSTAR and SPEX. The consistent use of this developed photoabsorption expression in both methods to address molecular abundances in the ISM, and clarify the existing controversy regarding the atomic–molecular fractions (García et al. 2011), will be the subject of a subsequent follow-up paper.

REFERENCES

Baldi, A., Ettori, S., Molendi, S., et al. 2012, A&A, 537, A142
Ballance, C. P., & Griffin, D. C. 2006, JPhB, 39, 3617
Bates, D. R. 1939, MNRAS, 100, 25
Berrington, K. A., Eissner, W. B., & Norrington, P. H. 1995, CoPhC, 92, 290
Bethe, H. A., & Salpeter, E. E. 1957, HDP, 35, 88
Burke, P. G. 2011, R-matrix Theory of Atomic Collisions (New York: Springer)
Cackett, E. M., Miller, J. M., Raymond, J., et al. 2008, ApJ, 677, 1233
Caldwell, C. D., Schaphorst, S. J., Krause, M. O., & Jimenez-Mier, J. 1994, JESRP, 67, 243
Canizares, C. R., Davis, J. E., Dewey, D., et al. 2005, PASP, 117, 1144
Cann, N. M., & Thakkar, A. J. 1992, PhRvA, 46, 5397
Cowan, R. D. 1981, The Theory of Atomic Structure and Spectra (Berkeley, CA: Univ. California Press)
de Vries, C. P., den Herder, J. W., Kaastra, J. S., et al. 2003, A&A, 404, 959
Dias, E. W. B., Chakraborty, H. S., Deshmukh, P. C., et al. 1997, PhRvL, 78, 4553
Drake, G. W. 1988, CaJPh, 66, 586

Einstein, A. 1905, AnP, 322, 132
Engstrom, L., & Litzen, U. 1995, JPhB, 28, 2565
Fano, U., & Cooper, J. W. 1968, RvMP, 40, 441
Froese Fischer, C. 1991, CoPhC, 64, 431
García, J., Mendoza, C., Bautista, M. A., et al. 2005, ApJS, 158, 68
García, J., Ramírez, J. M., Kallman, T. R., et al. 2011, ApJL, 731, L15
Gatuzz, E., García, J., Mendoza, C., et al. 2013, ApJ, 768, 60
Gorczyca, T. W., & Badnell, N. R. 1997, JPhB, 30, 3897
Gorczyca, T. W., & Badnell, N. R. 2000, JPhB, 33, 2511
Gorczyca, T. W., & McLaughlin, B. M. 2000, JPhB, 33, L859
Gorczyca, T. W., & Robicheaux, F. 1999, PhRvA, 60, 1216
Gorczyca, T. W., Robicheaux, F., Pindzola, M. S., Griffin, D. C., & Badnell, N. R. 1995, PhRvA, 52, 3877
Hansen, D. L., Hemmers, O., Wang, H., et al. 1999, PhRvA, 60, 2641
Henke, B. L., Gullikson, E. M., & Davis, J. C. 1993, ADNDT, 54, 181
Humphrey, P. J., Liu, W., & Buote, D. A. 2009, ApJ, 693, 822
Juett, A. M., Schulz, N. S., & Chakrabarty, D. 2004, ApJ, 612, 308
Kaastra, J. S., Werner, N., Herder, J. W. A. d., et al. 2006, ApJ, 652, 189
Krause, M. O. 1994, NIMPB, 87, 178
Liao, J.-Y., Zhang, S.-N., & Yao, Y. 2013, ApJ, 774, 116
McLaughlin, B. M., Ballance, C. P., Bowen, K. P., Gardenghi, D. J., & Stolte, W. C. 2013, ApJL, 771, L8
McLaughlin, B. M., & Kirby, K. P. 1998, JPhB, 31, 4991
Menzel, A., Benzaid, S., Krause, M. O., et al. 1996, PhRvA, 54, 991
Opacity Project Team. 1995, The Opacity Project, Vol. 1 (Bristol: IOP Publishing)
Opacity Project Team. 1997, The Opacity Project, Vol. 2 (Bristol: IOP Publishing)
Paerels, F., Brinkman, A. C., van der Meer, R. L. J., et al. 2001, ApJ, 546, 338
Pinto, C., Kaastra, J. S., Costantini, E., & de Vries, C. 2013, A&A, 551, A25
Pinto, C., Kaastra, J. S., Costantini, E., & Verbunt, F. 2010, A&A, 521, A79
Reilman, R. F., & Manson, S. T. 1979, ApJS, 40, 815
Schulz, N. S., Cui, W., Canizares, C. R., et al. 2002, ApJ, 565, 1141
Smith, F. T. 1960, PhRv, 118, 349
Starace, A. F. 1982, HDP, 31, 1
Stasińska, G., Prantzos, N., & Meynet, G. et al., (ed.) 2012, Oxygen in the Universe, EAS Publication Series, Vol. 54 (Paris: EDP Sciences)
Stolte, W. C., Lu, Y., Samson, J. A. R., et al. 1997, JPhB, 30, 4489
Takei, Y., Fujimoto, R., Mitsuda, K., & Onaka, T. 2002, ApJ, 581, 307
Verner, D. A., Ferland, G. J., Korista, K. T., & Yakovlev, D. G. 1996, ApJ, 465, 487
Verner, D. A., & Yakovlev, D. G. 1995, A&AS, 109, 125
Verner, D. A., Yakovlev, D. G., Band, I. M., & Trzhaskovskaya, M. B. 1993, ADNDT, 55, 233
Wuilleumier, F., & Krause, M. O. 1974, PhRvA, 10, 242